Journal of Thermal Analysis and Calorimetry (2020) 140:1057–1068
https://doi.org/10.1007/s10973-019-08840-2

The effect of arrangement type and pitch ratio on the performance of micro-pin-fin heat sinks

Ali Mohammadi[1,2] · Ali Koşar[2,3,4]

Received: 22 April 2019 / Accepted: 13 September 2019 / Published online: 26 September 2019

Abstract

This study focuses on comparison of in-line and staggered arrangements of circular micro-pin fins (MPF) in a rectangular micro-channel with the dimensions ($l' \times w' \times h'$) of 0.5 × 1.5 × 0.1 mm^3. The height (H) and diameter (D) of the MPFs are both 0.1 mm. Two horizontal (S_L) and vertical (S_T) distances of 0.15 and 0.3 mm are considered with each type of arrangement, which results in four in-line and four staggered configurations. The simulations are run at five Reynolds numbers (Re) between 20 and 150, and a constant heat flux (HF) of 30 W cm^{-2} was applied through the bottom surface of the MHS as well as the liquid interacting surfaces of MPFs. The results are analyzed using four evaluative parameters, namely pressure drop, friction factor (FF), Nusselt number (Nu) and thermal–hydraulic performance index (TPI). These parameters were significantly affected by the wake length behind MPFs. In cases with a large horizontal pitch ratio ($S_L/D = 3$), the wake length behind all columns (except the last one) could extend more (up to 2D) which in cases with the in-line arrangement typically resulted in higher pressure drop and FF (up to 10%) compared to similar cases with $S_L/D = 1.5$. In cases with $S_T/D = 3$, the larger available cross section among MPFs typically resulted in lower pressure drop (up to 36%) and Nu (up to 8%) compared to similar cases with $S_T/D = 1.5$. With the same S_L/D and S_T/D, staggered arrangements generally had higher pressure drop, FF and Nu (up to 56, 39 and 9%, respectively) compared to similar in-line arrangements. Finally, the best TPI was attained with staggered arrangements with $S_T/D = 1.5$ with 10% higher TPI compared to the reference case.

Keywords Micro-pin-fin heat sink · In-line · Staggered · Pitch ratio · Wake length · Thermal performance

List of symbols

A_c	Microchannel cross-sectional area (m^2)
A_{min}	Minimum available area (m^2)
D	Diameter of micro-pin fin (m)
D_h	Hydraulic diameter (m)
f	Friction factor
G	Mass flux (kg m^{-2} s^{-1})
H	Height of micro-pin fins (m)
H_d	Dense horizontal pitch ratio positioning
H_s	Sparse horizontal pitch ratio positioning
I	In-line
h	Convective heat transfer coefficient
h'	Height of microchannel (m)
L	Micro-pin fin length (m)
L_h	Hydrodynamic fully developed length (m)
l'	Length of the microchannel (m)
N	Number of micro-pin-fin rows
N_{col}	Number of micro-pin-fin columns
Nu	Nusselt number
P	Pressure [N m^{-2} (pa)]
p	Microchannel cross-sectional perimeter (m)
Q	Volumetric flow rate (m^3 s^{-1})
q	Heat (W)
Re	Reynolds number
S	Staggered
S_L	Horizontal distance between two micro-pin fins (m)

✉ Ali Koşar
kosara@sabanciuniv.edu

[1] Department of Mechanical and Manufacturing Engineering, University of Calgary, 2500 University Drive NW, Calgary, AB T2N 1N4, Canada

[2] Faculty of Engineering and Natural Sciences (FENS), Sabanci University, 34956 Tuzla, Istanbul, Turkey

[3] Nanotechnology Research and Application Center (SUNUM), Sabanci University, 34956 Tuzla, Istanbul, Turkey

[4] Center of Excellence for Functional Surfaces and Interfaces for Nanodiagnostics (EFSUN), Sabanci University, 34956 Tuzla, Istanbul, Turkey

S_T Vertical distance between two micro-pin fins (m)
T Temperature (k)
U Velocity (m s^{-1})
V_d Dense vertical pitch ratio positioning
V_s Sparse vertical pitch ratio positioning
w' Width of microchannel (m)

Abbreviation

HPR Horizontal pitch ratio
HTC Heat transfer coefficient
MHS Micro-heat sink
MPF Micro-pin fin
TPI Thermal–hydraulic performance index
VPR Vertical pitch ratio

Greek letters

ρ Density (kg m^{-3})
μ Dynamic viscosity (N s m^{-2})
ΔP Pressure drop [N m^{-2} (pa)]

Subscripts

in Inlet
m Mean
h.s. Heating surface
out Outlet

Introduction

Micro-heat sinks (MHS) have become very popular in recent years due to their extensive cooling and mixing capabilities [1]. Tuckerman and Pease [2] were the first ones to use liquid coolants in MHS in order to improve cooling performance. More than two decades later, Koşar et al. [3] employed MPFs for this purpose. They performed experiments with MPFs with H/D ratios of 1 and 2 and achieved lower FF with the latter case. In addition, staggered arrangement and diamond cross section of MPFs resulted in higher FF compared to the in-line arrangement and circular MPFs, respectively. Furthermore, thermal and hydrodynamic boundary layers affected the heat transfer coefficient (HTC) and FF where Re and H/D were the dominant factors [4].

Koşar and Peles [4] held end-wall effects responsible for the discrepancies between their results and the ones obtained from earlier correlations for a staggered arrangement of circular MPFs (H/D = 1 and 2.43, $5 < Re < 128$). With similar system and flow conditions using R-123 as the coolant, end-wall effects diminished for $Re > 100$ [5]. With a single circular MPF ($0.5 < H/D < 5$, $20 < Re < 150$) [6], end-wall effects and FF decreased with H/D and Re, whereas Nu increased with Re. Renfer et al. [7] considered circular MPFs (D = 100,[1] H = 100 and 200, $Re < 330$). For H/D = 2, the slope of pressure drop versus flow rate curve increased for $Re > 200$ which suggested a transition in flow patterns. In addition, heat transfer enhanced more in the case of H/D = 2 due to larger flow mixing, whereas dominant end-wall effects hindered generation of vortices and increased pressure drop for H/D = 1. Zhao et al. [8] considered staggered arrangements of circular, elliptical, diamond, square and triangular MPFs ($50 < Re < 1800$) and observed a general pattern where FF increased with Re due to dominating end-wall effects ($Re < 100$) and eddy dissipation ($Re > 300$).

The effect of MPF cross section has also been studied. Zhao et al. [8] mentioned that the triangular MPFs had the lowest FF in the laminar regime and the highest FF in the turbulent flow regimes compared to all other types of MPFs. A reverse pattern was reported with the elliptical ones. In an extension to this study, Guan et al. [9] considered triangular, circular and diamond MPFs ($100 < Re < 900$, HF < 150). At a fixed mass flux, pressure drops and FF increased with HF for all cases. However, FF curves reached a plateau beyond a certain Re. For both circular and diamond MPFs, HTCs increased with HF, whereas an increasing–decreasing trend was observed with the triangular MPFs. The values with the triangular case were always larger than the other cases. Koşar and Peles [10] considered circular, hydrofoil, cone-shaped and rectangular MPFs ($14 < Re < 720$). For all non-streamlined MPFs, Nu dependency on Re changed at a certain Re while for the hydrofoil case, the dependency level remained the same. The rectangular MPFs triggered more intense flow separation which increased the wake length, pressure drop and HTC. These studies suggested that the MPF cross section needs to be chosen based on the flow condition. Izci et al. [11] considered single MPF with different cross sections ($20 < Re < 120$, $200 <$ HF < 300). Rectangular MPFs had the largest HTC and Nu but also had the largest flow separations, which resulted in the largest pressure drop and FF. This highlights the other challenge where a good heat removal capacity is usually accompanied with a larger pressure drop penalty.

Beside the MPF cross section, some studies have considered the effect of MPF density. Koşar and Peles [10] reported larger HTCs and pressure drops with denser MPF configurations. Similarly, Koşar et al. [12] reported higher FF with staggered arrangements and denser configurations of circular, diamond and hydrofoil MPFs ($1 < Re < 2500$). The hydrofoil MPFs had lower pressure drop while diamond MPFs had significantly larger pressure drop. Hence,

[1] All length values are in micrometer, heat fluxes are in W cm^{-2} and coolants are water unless mentioned otherwise.

denser configuration are not favorable hydrodynamically but may enhance the thermal performance.

To manipulate the hydrodynamic penalty, recent studies have employed different MPF densities along the MHS. Rubio-Jimenez et al. [13] considered three of such designs with square, circular, elliptical and chamfered rectangular MPFs. The first one consisted of four sections with MPFs of different cross sections [H = 200 and length (L) = 75, 100 and 150]. The second one had four sections with rectangular MPFs but with varying heights from 100 to 300 μm. The third one had three sections with 200-μm-high MPFs. Heat dissipation rate was influenced by the ratio of heating area to the length of the sections with MPFs. The case with 100-μm-long rectangular MPFs had the best thermal performance. Pressure drop was significantly affected by the MPF shape and increased with the length of sections with MPFs. Sections with no MPFs were not recommended in this design. Gonzalez-hernandez et al. [14] studied another design with increasing MPF density along the channel. Two heights of 100 and 200 μm were considered for MHS, and for each of them, four cases with different MPF heights (20–50% of the channel height) were evaluated for flow rates between 72.765 and 145.53 mL min^{-1} [HF = 153.18 (from both top and bottom surfaces)]. For the highest flow rate, the 200 μm MHS with 60-μm-high MPFs had the best temperature uniformity with only 2.24 k difference in different regions. For the lowest flow rate, the 200 μm MHS with 80-μm-high MPFs had the best temperature uniformity with only 2.91 k temperature difference. This shows the importance of proper geometry selection based on the flow condition. In addition, for both flow rates and for both MHS heights, pressure drop increased with H which shows the same challenge between heat transfer gain and pressure drop penalty.

To study the effect of gap size, Liu et al. [15] considered in-line and staggered arrangements of circular MPFs ($250 < H < 1000$) in a 1-mm-high MHS ($25 < Re < 800$) where FF increased with the gap size. In-line arrangements had lower FF as a result of fewer interactions among generated vortices. Roth et al. [16] considered circular MPFs ($65 < D < 100$, $251.6 < H < 264.4$) with a fixed gap size of 50 μm ($9 < Re < 238.4$). At lower Re, heat transfer increased with D. In addition, Nu increased sharply with Re and reached a plateau.

To study the effect of pitch ratios, John et al. [17] considered in-line arrangements of circular and square MPFs ($50 < Re < 500$). Horizontal and vertical distances between MPFs (HPD and VPD) were varied between 350 and 650 μm and between 150 and 300 μm, respectively. For the circular MPFs, pressure drop and thermal resistance were significantly affected by HPD. Liu et al. [18] considered pitch ratios between 0.9 and 1.1 in different in-line and staggered arrangements of circular MPFs. Nu decreased and FF slightly changed with pitch ratios. Sluggish flow regions were highlighted as the reason for over-prediction of earlier correlations for FF and Nu at low Re.

To study the effect of nanoparticles, Bahiraei et al. [19] considered circular MPFs (H = 200, 400, 600 and 800, and D = 600, 900 and 1200) in a 1-mm-high MHS using graphene nano-platelets. The bottom surface temperature and thermal resistance decreased, and the pumping power and temperature distribution uniformity increased with particle concentration, H and D. Although a significantly better thermal performance was reported when employing nanoparticles, pressure drop didn't change much. Bahiraei et al. [20] also considered a step microchannel design which had 20 parallel channels (L = 29.23 mm and W = 1.2 mm) using Al_2O_3–water as the coolant. The parallel channels had a uniform flow which ensured a uniform temperature distribution ($400 < Re < 1000$). The surface temperature decreased and the power consumption increased with either Re and particle concentration.

Although many studies have focused on the effect of geometrical specifications of MPFs and the flow conditions, the results are not easily comparable due to high number of variables. In an effort to do a systematic study, Mohammadi and Koşar [21, 22] did a two-part study considering ten in-line [21] and ten staggered [22] arrangements of circular MPFs (D = 50, 100 and 200). Two horizontal and vertical pitch ratios (HPR and VPR) of 1.5 and 3 were considered [$20 < Re < 160$, HF = 30 (through the bottom surface)]. For the in-line arrangements, Nu decreased and pressure drops increased with both VPR and H/D. Besides, pressure drops increased and thermal performance indices (TPIs) decreased with HPR. Distinct decreasing/increasing trends were observed for TPIs with both VPRs. For the staggered arrangements, both Nu and pressure drops were significantly affected by the wake length behind MPFs which was intensified with both Re and HPR. The velocity gradients became milder, pressure drops decreased and Nu increased with VPR. For H/D = 1 and 2, TPIs had an increasing–decreasing trend with Re with the turning point somewhere between Re = 40 and 80.

Although the amount of heat flux through the bottom surface of all arrangements in these two studies [21, 22] was the same, the generated heat through MPFs was different. Hence, to ensure a fair comparison, the heat flux through all heating surfaces are set to be 30 W cm^{-2} in this study. In addition, to further simplify the comparison, only the arrangements with H/D = 1 are considered which leaves the arrangement type (in-line or staggered), HPR (1.5 or 3) and VPR (1.5 or 3) as the variables. Hence, four in-line and four staggered arrangements of circular MPFs

are considered. Assuming a single-phase laminar flow, the simulations were run at five *Re* equal and below 150 which results in a total of 40 study cases.

Geometrical modeling and methodology

Four in-line and four staggered arrangements of circular MPFs in a rectangular microchannel with the dimensions of $5 \times 1.5 \times 0.1$ mm^3 are considered. The diameter and height of MPFs in all cases are 0.1 mm. Two values (0.15 and 0.3 mm) are considered for both the horizontal (S_L) and vertical (S_T) distances between MPFs. This results in HPR (S_L/D) and VPR (S_H/D) of 1.5 and 3, respectively. These eight configurations are labeled in Table 1 for an easier reference. *I* and *S* on the first letter stand for in-line and staggered arrangements, respectively. *V* and *H* on the second and forth letters stand for vertical and horizontal directions, respectively. Finally, *d* and *s* on either the third or fifth letters stand for dense (0.15 mm) and sparse (0.3 mm) spacing. For instance, IV_dH_d refers to an in-line arrangement with a dense vertical and a dense horizontal spacing. For all cases, a constant number of 30 MPFs is considered for a better comprehensive comparison. Hence, in cases with S_T/D of 1.5, three columns of MPFs exist, while in cases with S_T/D of 3, six MPF columns exist. For the IV_dH_d and IV_dH_s configurations, an additional three MPFs are needed behind the last column of MPFs to have a total of 30 MPFs, as shown in Fig. 1. The total heating area in each case is 8.2×10^{-6} m^2, which consists of a 7.265×10^{-6} m^2 microchannel-free base area and a 9.425×10^{-7} m^2 MPF surface area.

For all cases, the initial section is MPF-free to let the flow become hydrodynamically fully developed before encountering the first column of MPFs. This length is calculated as [23]:

$$L_h = 0.05 D_h Re \tag{1}$$

where D_h is the hydraulic diameter which depends on the channel inlet cross-sectional area, A_c, and its perimeter, *p*:

Table 1 Geometrical specifications of all configurations

Label	*H*/*D*	S_T/D	S_L/D
IV_dH_d	1	1.5	1.5
IV_dH_s	1	1.5	3
IV_sH_d	1	3	1.5
IV_sH_s	1	3	3
SV_dH_d	1	1.5	1.5
SV_dH_s	1	1.5	3
SV_sH_d	1	3	1.5
SV_sH_s	1	3	3

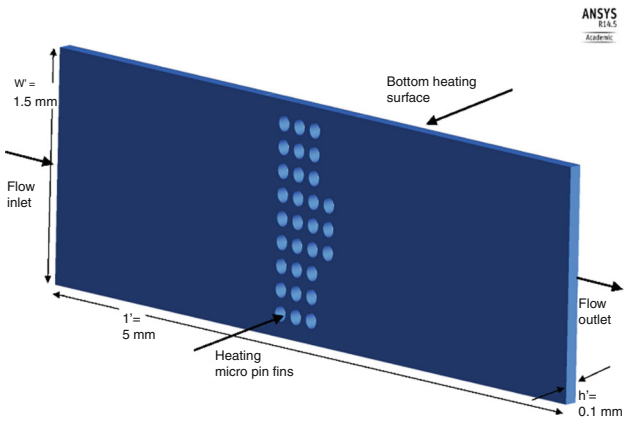

Fig. 1 Three-dimensional model of the IV_dH_d configuration

$$D_h = \frac{4A_c}{p} \tag{2}$$

Reynolds number is calculated as:

$$Re = \frac{\rho U_{in} D_h}{\mu} \tag{3}$$

where ρ and μ are the fluid (water) density and dynamic viscosity at $T = 300$ K, respectively, and U_{in} is the fluid inlet velocity. A distance of 10D is considered behind the last column of MPFs to ensure the vortices are significantly damped.

Numerical modeling

For each configuration, the simulations are run at five *Re* values (20, 40, 80, 120 and 150). The fluid inlet temperature is 300 K while a constant HF = 30 W cm^{-2} is applied through the bottom section of the microchannel and the liquid interacting surfaces of the MPFs. The top and side surfaces of the microchannel are thermally isolated. The outlet boundary opens to the atmosphere. Thermophysical properties (density, thermal conductivity, specific heat and dynamic viscosity) of the fluid are set to vary with temperature for higher accuracy [24]. Table 2 summarizes the boundary conditions:

The set of steady compressible continuity, momentum and energy equations (Eqs. 4–6) were solved using the ANSYS FLUENT 14.5 software. Each of the simulations took about 20 h on average to satisfy the residual criterion of 10^{-5} using workstations with double-processor Intel Xenon 2.4 GHz CPU and 12 GB of RAM. The least-square cell-based interpolation and the second-order upwind methods were used to resolve the gradients of solution variables and interpolation of the field variables, respectively:

Table 2 Boundary conditions

Wall section	Boundary conditions
Inlet section	$U_x = U_{in}$, $U_y = U_z = 0$ and $T_{x=0,y,z} = T_{in} = 300\,K$
Outlet section	$P_{x=L,y,z} = P_{atm}$
MC bottom surface	$U_{x,y,z=0} = 0$ and $(q \cdot \hat{n})_{x,y,z=0} = 30\ W\ cm^{-2}$
MC upper surface	$U_{x,y,z=h'} = 0$ and $(q \cdot \hat{n})_{x,y,z=0} = 0$
MC side walls	$U_{x,y=0,z} = U_{x,y=w',z} = 0$ and $(q \cdot \hat{n})_{x,y=0,z} = (q \cdot \hat{n})_{x,y=w',z} = 0$
MPFs liquid interacting surfaces	$U_{fin.surface} = 0$ and $(q \cdot \hat{n})_{fin.surface} = 30\ W\ cm^{-2}$

$$\frac{\partial(\rho u)}{\partial x} + \frac{\partial(\rho v)}{\partial y} + \frac{\partial(\rho w)}{\partial z} = 0 \tag{4}$$

$$\begin{aligned}
\frac{\partial(\rho u^2)}{\partial x} + \frac{\partial(\rho uv)}{\partial y} + \frac{\partial(\rho uw)}{\partial z} &= -\frac{\partial P}{\partial x} + \frac{1}{Re}\left(\frac{\partial \tau_{xx}}{\partial x} + \frac{\partial \tau_{xy}}{\partial y} + \frac{\partial \tau_{xz}}{\partial z}\right) \\
\frac{\partial(\rho uv)}{\partial x} + \frac{\partial(\rho v^2)}{\partial y} + \frac{\partial(\rho vw)}{\partial z} &= -\frac{\partial P}{\partial y} + \frac{1}{Re}\left(\frac{\partial \tau_{yx}}{\partial x} + \frac{\partial \tau_{yy}}{\partial y} + \frac{\partial \tau_{yz}}{\partial z}\right) \\
\frac{\partial(\rho uw)}{\partial x} + \frac{\partial(\rho vw)}{\partial y} + \frac{\partial(\rho w^2)}{\partial z} &= -\frac{\partial P}{\partial z} + \frac{1}{Re}\left(\frac{\partial \tau_{zx}}{\partial x} + \frac{\partial \tau_{zy}}{\partial y} + \frac{\partial \tau_{zz}}{\partial z}\right)
\end{aligned} \tag{5}$$

$$\begin{aligned}
\frac{\partial(uE)}{\partial x} + \frac{\partial(vE)}{\partial y} + \frac{\partial(wE)}{\partial z} &= -\frac{\partial(uP)}{\partial x} - \frac{\partial(vP)}{\partial y} - \frac{\partial(wP)}{\partial z} \\
&- \frac{1}{Re \times Pr}\left(\frac{\partial q_x}{\partial x} + \frac{\partial q_y}{\partial y} + \frac{\partial q_z}{\partial z}\right) \\
&- \frac{1}{Re}\left(\frac{\partial}{\partial x}\left(u\tau_{xx} + v\tau_{xy} + w\tau_{xz}\right) + \frac{\partial}{\partial y}\left(u\tau_{yx} + v\tau_{yy} + w\tau_{yz}\right)\right. \\
&\left. + \frac{\partial}{\partial z}\left(u\tau_{zx} + v\tau_{zy} + w\tau_{zz}\right)\right).
\end{aligned} \tag{6}$$

Grid sensitivity analysis

The microchannel length is divided into three sections: (1) before MPFs, (2) MPF section and (3) behind MPFs, as presented in Table 3 for different configurations. In the first and third sections, structured rectangular grids and in the second section, unstructured tri/rectangular grids are used. In addition, to capture the velocity and temperature gradients close to the heating sections, inflation layers are used to refine the grid size in these regions.

Table 4 presents the details of the three grid networks used to test sensitivity of the results to grid size for the IV_dH_d configuration. The maximum obtained static temperature in the whole domain is used to compare these cases. Since the results obtained by the second and third grid networks are close, the second network is used for this case. Similar networks are used for all the other configurations.

Table 3 Length of different sections

Case	First section/mm	Second section/mm	Third section/mm
IV_dH_d	2	0.9	2.1
IV_dH_s	1.8	1.4	1.8
IV_sH_d	1.8	1.2	2
IV_sH_s	1.6	2	1.4
SV_dH_d	2.1	0.8	2.1
SV_dH_s	1.95	1.1	1.95
SV_sH_d	1.875	1.25	1.875
SV_sH_s	1.5	2	1.5

Validation of numerical results

To validate the numerical model, experimental data of Koşar and Peles [10] (2CLD case which includes 28 columns and 12 rows of circular MPFs in a staggered arrangement with S_T = 150 μm and S_L = 300 μm) are used (by applying the same operating conditions). Figure 2a, b compares the experimental data and the results obtained from simulation. For the pressure data, the average and maximum differences are 13.9% and 23.4%, respectively. For the temperature difference between the inlet and outlet sections, the average and maximum differences are 5.1% and 10.2%, respectively, which provide sufficiently acceptable accuracy.

Post-processing of the results

The hydrodynamic performance of MHS is assessed with two parameters: (1) pressure drop and (2) friction factor. These are expressed in Eqs. 8 and 9, respectively [12]:

Table 4 Grid sensitivity analysis

Case no.	Nodes	Elements	$T_{static\text{-}max.}$/K	Dif./%
1	54,967	145,416	322.102	0
2	269,733	597,975	326.913	1.47
3	630,330	1,135,318	326.972	0.02

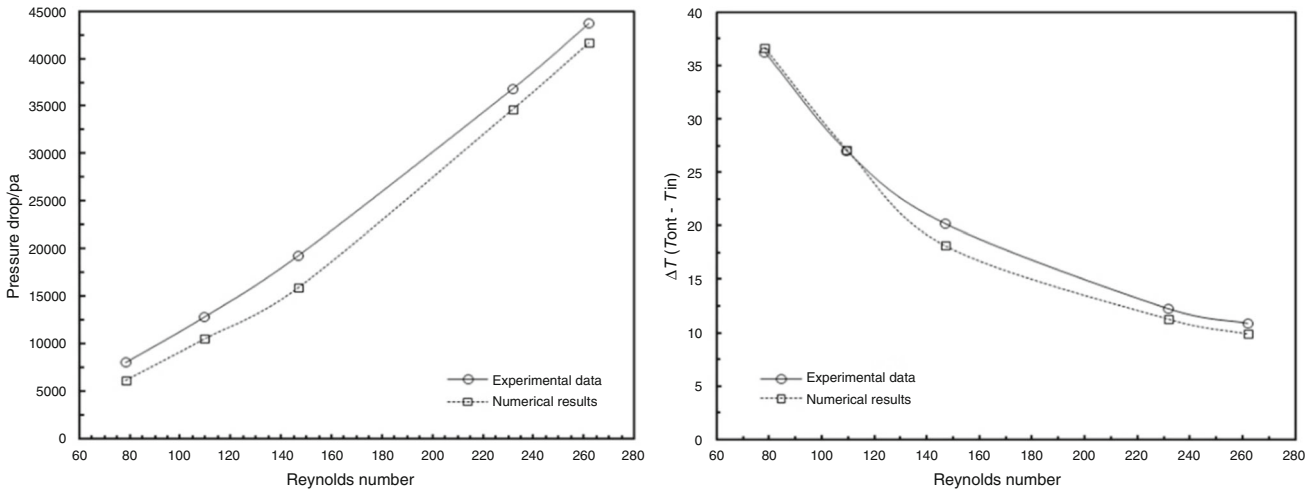

Fig. 2 Comparison of the simulation data with the results of Koşar and Peles [10]—ΔP and ΔT versus Re

$$P_{\text{in}} = \frac{\int_{\text{in}} P \, \mathrm{d}A}{A_{\text{in}}} \tag{7a}$$

$$P_{\text{out}} = \frac{\int_{\text{out}} P \, \mathrm{d}A}{A_{\text{out}}} \tag{7b}$$

$$\Delta P = P_{\text{in}} - P_{\text{out}} \tag{8}$$

$$f_{\text{exp}} = \frac{2\rho \Delta P}{N_{\text{col}} G^2} \tag{9}$$

where ρ is the volumetric averaged density of the fluid, N_{col} is the number of MPF columns and G is the mass flux, which is expressed as [12]:

$$G = \frac{\rho Q}{A_{\min}} \tag{10}$$

where $A_{\min}$ for the in-line and staggered arrangements is obtained with Eqs. 11a and 11b, respectively [12]:

$$A_{\min} = (w' - ND)h' \tag{11a}$$

$$A_{\min} = \frac{S_{\text{T}} - D}{S_{\text{T}}} w' h' \tag{11b}$$

The thermal performance of the systems is assessed using Nusselt number. For this purpose, the inlet, outlet, average and wall surface temperatures are calculated using Eqs. 12a–12d, respectively:

$$T_{\text{in}} = \frac{\int_{\text{in}} T \, \mathrm{d}A}{A_{\text{in}}} \tag{12a}$$

$$T_{\text{out}} = \frac{\int_{\text{out}} T \, \mathrm{d}A}{A_{\text{out}}} \tag{12b}$$

$$T_{\text{m}} = \frac{T_{\text{in}} + T_{\text{out}}}{A_{\text{h.s.}}} \tag{12c}$$

$$T_{\text{h.s.}} = \frac{\int_{\text{h.s.}} T \, \mathrm{d}A}{A_{\text{h.s.}}} \tag{12d}$$

which leads to obtaining heat transfer coefficient and Nusselt numbers:

$$h = \frac{q}{A_{\text{h.s.}}(T_{\text{h.s.}} - T_{\text{m}})} \tag{13}$$

$$Nu = \frac{hD_{\text{h}}}{k} \tag{14}$$

where q is the heat input and k is the volumetric averaged thermal conductivity of the fluid.

Finally, the thermal–hydraulic performance index (TPI) is used to take both thermal and hydrodynamic performances into account [25]. It represents the ratio of the normalized Nusselt number over the third root of the normalized friction factor. The normalization is done using the values obtained for the $\text{IV}_{\text{d}}\text{H}_{\text{d}}$ configuration at a constant pumping power:

$$\text{TPI} = \frac{Nu/Nu_{\text{IV}_{\text{d}}\text{H}_{\text{d}}}}{(f/f_{\text{IV}_{\text{d}}\text{H}_{\text{d}}})^{1/3}}. \tag{15}$$

Results and discussion

Hydrodynamic performance

As the fluid passes over the sections with MPFs, the streamlines get disturbed. At a sufficiently high Re, they separate from the surface of the obstacle which creates a negative pressure gradient behind MPFs. In addition to the MPF cross section, the number of MPFs, arrangement type and Re affect the pressure drop and friction factors. In the

following sections, the effects of Re, S_L/D, S_T/D and the arrangement type are analyzed in detail.

Pressure drop

Figure 3 shows the pressure drop values as a function of Re, and Table 5 presents the same data for an easier reference. For all cases, pressure drop increases with Re which is mainly attributed to larger wake length behind MPFs, Fig. 4.

Figure 5 depicts the velocity profiles of the IV_dH_d and IV_dH_s configurations at the mid-span height at Re = 80. Table 6 presents the wake length behind each MPF column in these two configurations (the values nondimensionalized by D) as well as the ratio of the wake length of these two cases behind each MPF column. As can be seen in Fig. 5, the wake behind the first two columns of the IV_dH_d configuration is restricted with the MPF of the next column and cannot extend much whereas in the IV_dH_s configuration, such restriction does not exist. This can be noticed in the wake length ratios which varies between 0.43 (Re = 20) to 3.71 (Re = 150) and is mostly above 1.8 for the first two columns whereas for the third column, the ratio varies between 0.38 (Re = 20) to 0.86 (Re = 120). A similar comparison can be made between the IV_sH_d and IV_sH_s configurations which has the same arrangement type and VPR.

For staggered arrangements with the same VPR, distinct patterns are seen with VPR = 1.5 and 3. For VPR = 1.5, pressure drop values are very close for the SV_dH_d and SV_dH_s configurations. The former has higher values at Re = 20, 40 and 80, whereas the latter has higher values at Re = 120 and 150. For VPR = 3, the SV_sH_d configuration has higher pressure drops compared to the SV_sH_s configuration for all Re which shows an opposite trend to the in-line arrangements.

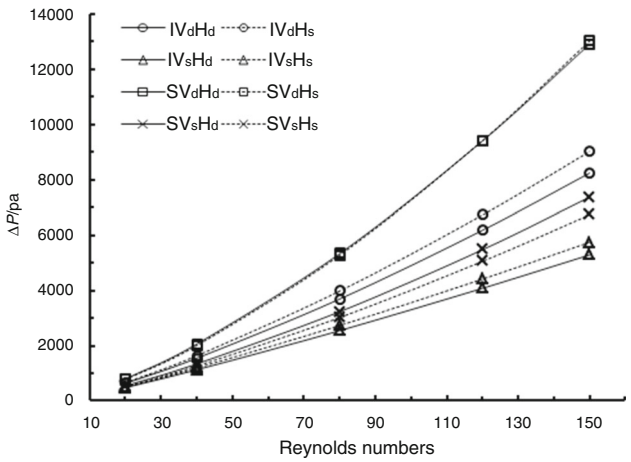

Fig. 3 Pressure drop versus Re

For configurations with the same arrangement type and HPR, such as the IV_dH_d and IV_sH_d configurations, the one with VPR = 1.5 has significantly higher pressure drop which is attributed to larger velocity gradients as a result of less available cross section, Fig. 6. A similar comparison can be made for all the other similar pairs.

Finally, for configurations with the same VPR and HPR but different arrangement types, such as the IV_dH_d and SV_dH_d configurations, the one with the staggered arrangement has higher pressure drops. The difference is high enough to result in a larger pressure drop even when comparing a staggered arrangement with HPR = 1.5 (e.g., SV_dH_s), to an in-line arrangement with VPR = 3 (e.g., IV_dH_d). This is attributed to more numerous regions with significant velocity gradients with the staggered configuration (Fig. 7).

Friction factor

Friction factor directly depends on the density and pressure drop and is inversely dependent on the number of MPF columns and square root of mass flux. The number of MPF columns for the configurations with VPR = 1.5 is 3 (neglecting the additional MPFs in the last column of in-line arrangements), whereas N_{col} is 6 for the configurations with VPR = 3. Figure 8 illustrates FF variation with configuration type at different Re values, and Table 7 presents the same data for a better comparison. For each configuration, FF decreases with Re. This reduction, despite the increase in ΔP with Re, suggests that mass flux has a dominant effect.

The comparison between configuration pairs with the same arrangement type and VPR resembles the related comparison of ΔP in the previous section. The number of N_{col} is not important in this comparison as it is the same for each pair leg. For the in-line arrangements, the configurations with HPR = 3 have larger FF as a result of larger ΔP. For staggered arrangements, two patterns exist. For VPR = 1.5, the FF values are very close to each other such that the SV_dH_d configuration has higher values at Re = 20, 40 and 80 and the SV_dH_s configuration has larger FF at the other two Re. For VPR = 3, the SV_sH_d configuration has larger FF.

The comparison between the configurations with the same arrangement type and HPR is more delicate as N_{col} in the second leg of the pair is twice the first one. For the in-line arrangements with either the dense or sparse HPR, the configuration with VPR = 3 has larger FF at Re = 20 and 40 and the configuration with VPR = 1.5 has larger FF at higher Re. The additional three MPFs added to the IV_dH_d and IV_dH_s configurations make a more detailed comparison difficult. For the staggered arrangement with either the

Table 5 Pressure drops for different configurations at different *Re* values

Re/conf.	IV_dH_d	IV_dH_s	IV_sH_d	IV_sH_s	SV_dH_d	SV_dH_s	SV_sH_d	SV_sH_s
20	631.63	662.95	478.19	504.23	793.22	771.46	545.51	515.64
40	1546.90	1642.39	1129.13	1200.33	2063.87	2012.39	1343.82	1265.37
80	3689.34	3980.91	2545.57	2732.78	5332.84	5276.16	3231.15	3021.68
120	6179.59	6732.27	4080.75	4413.52	9405.11	9418.86	5475.69	5057.15
150	8238.42	9021.60	5289.05	5748.31	12,905.17	13,025.51	7372.63	6733.28

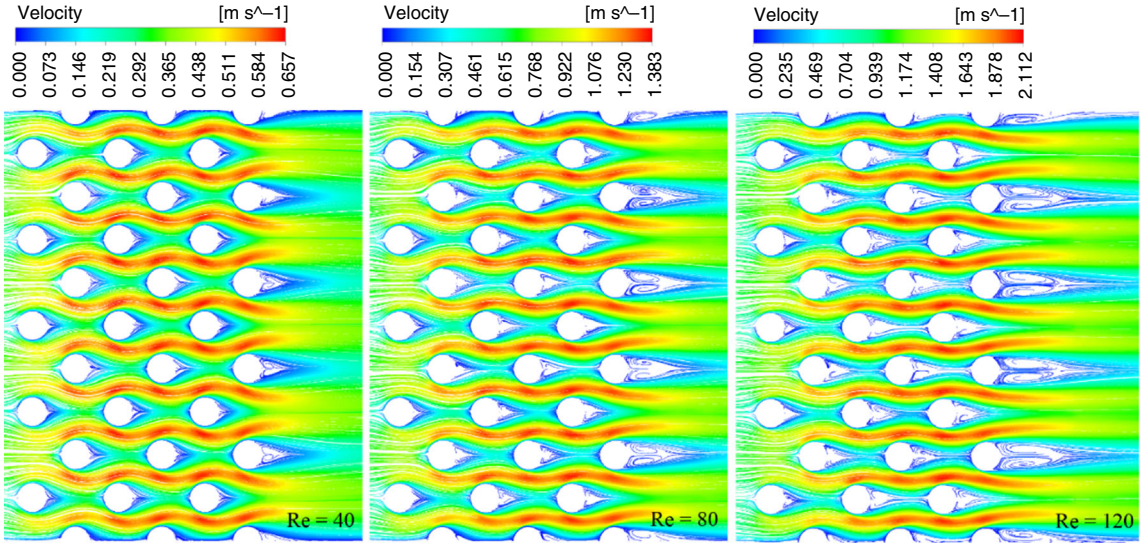

Fig. 4 Velocity profiles for the SV_sH_d configuration at the mid-span height at *Re* = 40, 80 and 120

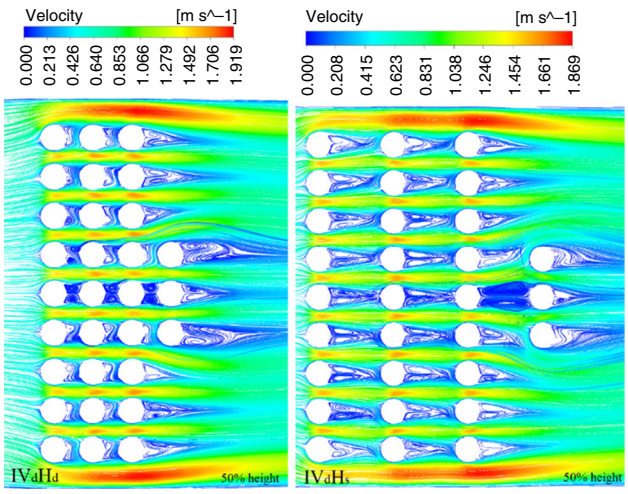

Fig. 5 Velocity profiles of the IV_dH_d and IV_dH_s configurations at the mid-span height (*Re* = 80)

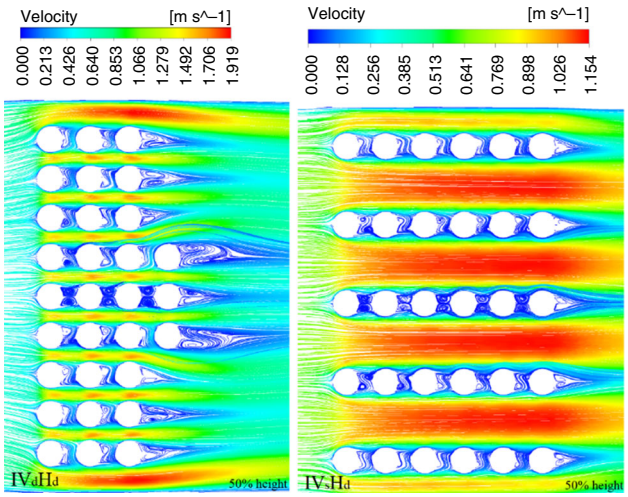

Fig. 6 Velocity profiles of the IV_dH_d and IV_sH_d configurations at the mid-span height (*Re* = 80)

dense or sparse HPR, the configuration with VPR = 3 has a higher FF at all *Re*.

The comparison of the configuration pairs with the same HPR and VPR but different arrangement types suffers from the additional MPFs as well. Therefore, only the IV_sH_d and SV_sH_d, and the IV_sH_s and SV_sH_s configurations are compared where the ones with the staggered arrangement have larger FF in each pair.

Table 6 Nondimensionalized wake lengths for the IV_dH_d and IV_dH_s configurations and their ratio

Re/conf.	Column 1			Column 2			Column 3		
	IV_dH_d	IV_dH_s	Ratio	IV_dH_d	IV_dH_s	Ratio	IV_dH_d	IV_dH_s	Ratio
20	0.54	0.23	0.43	0.54	0.23	0.43	0.62	0.23	0.38
40	0.54	1.00	1.86	0.54	1.00	1.86	0.92	0.77	0.83
80	0.54	1.46	2.71	0.54	1.46	2.71	1.54	1.23	0.80
120	0.54	2.00	3.71	0.54	2.00	3.71	2.15	1.85	0.86
150	0.54	2.00	3.71	0.54	2.00	3.71	2.15	1.77	0.82

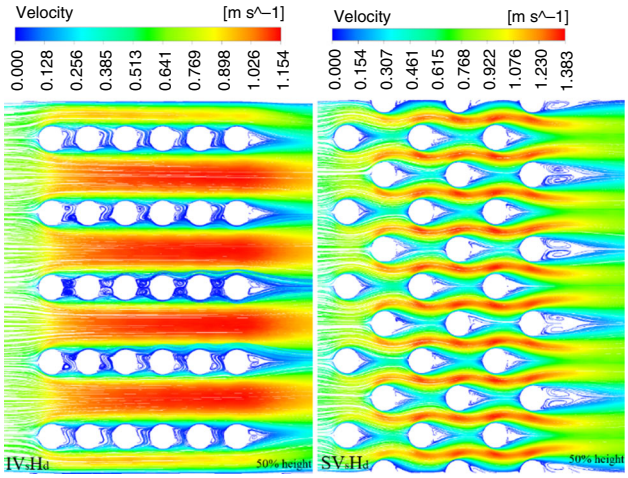

Fig. 7 Velocity profiles of the IV_sH_d and SV_sH_d configurations at the mid-span height (*Re* = 80)

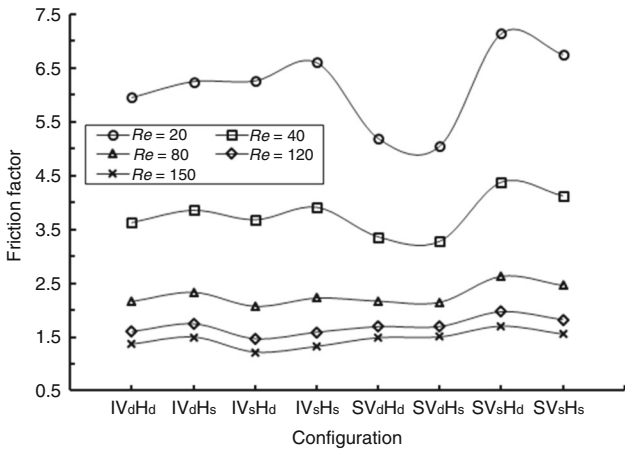

Fig. 8 Friction factor versus configuration type at different *Re* values

Thermal performance

Nusselt number is used as the parameter to compare the thermal performance. It depends on the convective HTC, D_h and k. Since D_h is the same for all cases and k does not change significantly, *Nu* comparison mainly depends on h, which itself is a function of q, $A_{h.s.}$ and $(T_{h.s.} - T_m)$. Since q and $A_{h.s.}$ are equal for all configurations, the comparison of h or *Nu* mainly depends on ΔT.

Figure 9 and Table 8 present the *Nu* for different configurations. For each configuration, *Nu* increases with *Re*. The comparison between configuration pairs with the same arrangement type and VPR shows that at *Re* = 80, 120 and 150, the configurations with HPR = 3 have higher *Nu* which is due to a smaller difference between the fluid and heating surface temperatures. At *Re* = 20 and 40, the pattern is not unanimous as the temperature difference between cases with HPR = 1.5 and 3 are close and surpass each other with no regular pattern.

The comparison of the configuration pairs with the same arrangement type and HPR shows that the configurations with the VPR = 1.5 have higher *Nu* (with no exception) which is also due to a smaller temperature difference between the fluid and heating surfaces (as a result of less space between MPFs and hotter regions of fluid). Finally, the comparison of the configuration pairs with the same HPR and VPR shows that the staggered arrangements have higher *Nu* which can be attributed to higher mixing and thus less temperature difference between the heating surfaces and the liquid. Figure 10 shows the temperature profiles at the 20% and 50% height of the SV_sH_s configuration at *Re* = 80. It is seen that the flow washes away the heat generated through the MPF surfaces toward the end of the channel.

Table 7 Friction factor for different configurations at different *Re* values

Re/conf.	IV_dH_d	IV_dH_s	IV_sH_d	IV_sH_s	SV_dH_d	SV_dH_s	SV_sH_d	SV_sH_s
20	5.951	6.246	6.259	6.599	5.190	5.047	7.138	6.747
40	3.629	3.853	3.680	3.912	3.362	3.279	4.379	4.123
80	2.160	2.331	2.070	2.222	2.168	2.145	2.627	2.457
120	1.602	1.745	1.469	1.589	1.693	1.696	1.972	1.821
150	1.369	1.499	1.221	1.327	1.489	1.503	1.702	1.554

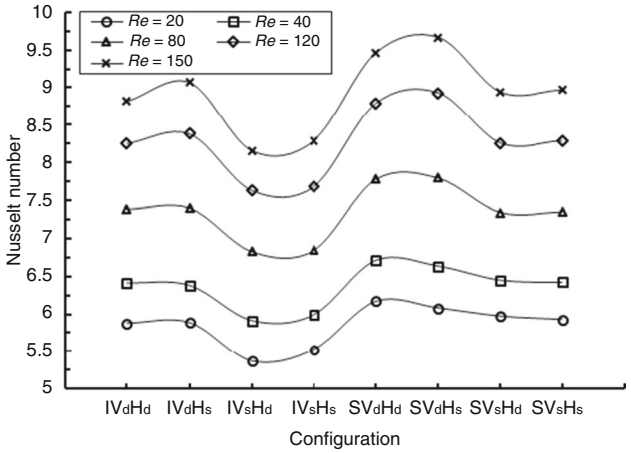

Fig. 9 Nusselt number versus configuration type at different *Re* values

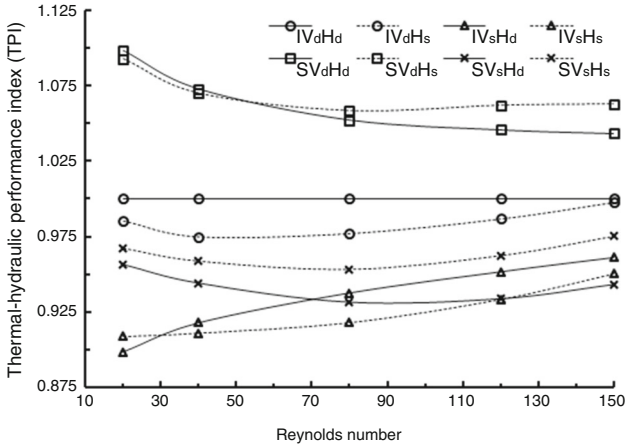

Fig. 11 Thermal performance index (TPI) of different configurations versus *Re*

Thermal–hydraulic performance

Figure 11 illustrates the thermal–hydraulic performance index (TPI) as a function of *Re*, and Table 9 presents the same data. Since FF and Nu of the IV_dH_d configuration are used as the normalizing factors, the TPI for this case remains 1 for all *Re*. The TPI of five configurations is below 1. For the in-line configurations, the patterns are mostly increasing which indicate that as *Re* increases, the heat removal gain of the systems are better compared to the pressure drop penalty (and FF). The only exception is the IV_dH_s configuration between *Re* = 20 and 40. Comparing the configuration pairs with the same VPR, the configuration with HPR = 1.5 has a larger TPI which is mainly due to their higher FF. The only exception is between the IV_sH_d and IV_sH_s configurations at *Re* = 20.

Table 8 Nusselt number for different configurations at different *Re* values

Re/conf.	IV_dH_d	IV_dH_s	IV_sH_d	IV_sH_s	SV_dH_d	SV_dH_s	SV_sH_d	SV_sH_s
20	5.880	5.889	5.373	5.530	6.171	6.082	5.975	5.932
40	6.416	6.381	5.915	5.992	6.711	6.636	6.448	6.420
80	7.383	7.398	6.824	6.841	7.779	7.796	7.340	7.347
120	8.254	8.380	7.631	7.683	8.793	8.932	8.259	8.291
150	8.818	9.068	8.157	8.292	9.462	9.669	8.942	8.973

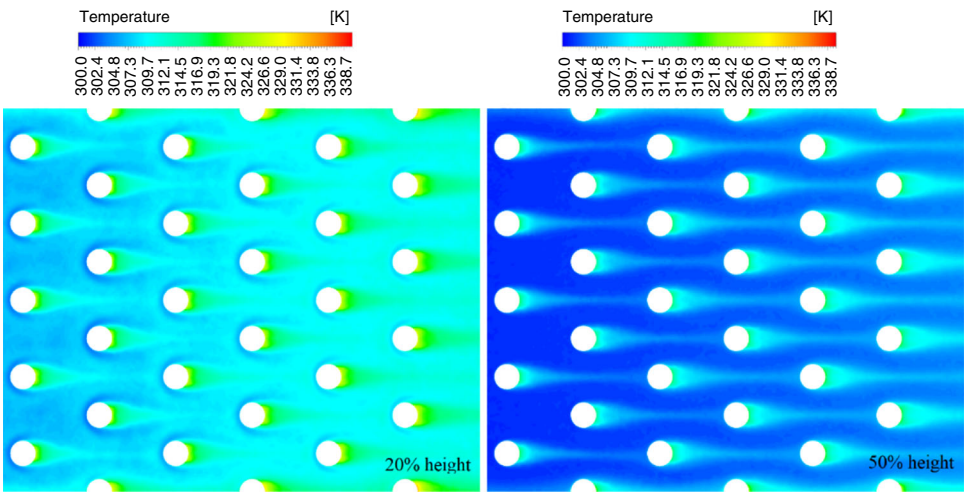

Fig. 10 Temperature profiles of the SV_sH_s configuration at 20% and 50% heights (*Re* = 80)

Table 9 TPI values for different configurations at different *Re* values

Re/conf.	IV_dH_d	IV_dH_s	IV_sH_d	IV_sH_s	SV_dH_d	SV_dH_s	SV_sH_d	SV_sH_s
20	1.000	0.985	0.898	0.909	1.098	1.093	0.956	0.967
40	1.000	0.975	0.918	0.911	1.073	1.070	0.944	0.959
80	1.000	0.977	0.938	0.918	1.052	1.058	0.931	0.953
120	1.000	0.987	0.952	0.933	1.046	1.062	0.934	0.963
150	1.000	0.998	0.961	0.950	1.043	1.063	0.943	0.975

For the staggered configurations, two patterns are seen with VPR. For VPR = 1.5, TPI mostly drops with *Re* which indicates a larger effect of the pressure drop (and FF) compared to the gain of heat transfer. The only exception is the SV_dH_s configuration at *Re* = 150. Despite this decreasing trend, TPIs of the SV_dH_s and SV_dH_s configurations are the only ones above 1 for all *Re* which is a result of relatively high Nu and low FF. For VPR = 3, the patterns for both configurations are decreasing at *Re* = 20, 40 and 80 and increasing at *Re* = 120 and 150. Comparing the configurations pairs with the same VPR, the ones with HPR = 3 mostly have the higher TPI. The exception is the SV_dH_d and SV_dH_s configurations at *Re* = 20 and 40.

Summary and conclusions

In this study, the hydrodynamic and thermal performances of eight MHS with different in-line and staggered arrangements of MPFs were compared, where the focus was on the effect of arrangement type and pitch ratios. These parameters changed the available cross-sectional area at the MPF locations and affected the wake length behind MPFs which both affect the evaluative parameters. The findings of this study can be summarized as follows:

- A larger VPR, which provides a larger available cross section, generally results in lower pressure drops and higher *Nu*.
- A larger HPR allows the wake to extend more which generally results in higher pressure drops, FF and *Nu*.
- With the same HPR and VPR, staggered arrangements generally result in higher pressure drops, FF and *Nu*.
- The best overall TPI was achieved with the staggered arrangement with VPR = HPR = 1.5. This configuration has 9.3% (at *Re* = 20), 7% (*Re* = 40) and about 6% (*Re* = 80, 120 and 150) higher TPI compared to the reference case.

References

1. Mohammadi A, Koşar A. Review on heat and fluid flow in micro pin fin heat sinks under single-phase and two-phase flow conditions. Nanoscale Microscale Thermophys Eng. 2018;22(3):153–97.
2. Tuckerman DB, Pease RFW. High-performance heat sinking for VLSI. IEEE Electron Dev Lett. 1981;2(5):126–9.
3. Koşar A, Mishra C, Peles Y. Laminar flow across a bank of low aspect ratio micro pin fins. J Fluids Eng. 2005;127(5):419–30.
4. Koşar A, Peles Y. Thermal-hydraulic performance of MEMS-based pin fin heat sink. J Heat Transf. 2006;128(2):121–31.
5. Koşar A, Peles Y. Convective flow of refrigerant (R-123) across a bank of micro pin fins. Int J Heat Mass Transf. 2006;49(17–18):3142–55.
6. Koz M, Ozdemir MR, Koşar A. Parametric study on the effect of end walls on heat transfer and fluid flow across a micro pin-fin. Int J Therm Sci. 2011;50(6):1073–84.
7. Renfer A, Tiwari MK, Brunschwiler T, Michel B, Poulikakos D. Experimental Investigation into vortex structure and pressure drop across microcavities in 3D integrated electronics. Exp Fluids. 2011;51(3):731–41.
8. Zhao H, Liu Z, Zhang C, Guan N, Zhao H. Pressure drop and friction factor of a rectangular channel with staggered mini pin fins of different shapes. Exp Therm Fluid Sci. 2016;71:57–69.
9. Guan N, Jiang G, Liu ZG, Zhang CW. Effects of heating load on flow resistance and convective heat transfer in micro-pin-fin heat sinks with different cross-section shapes. Exp Heat Transf. 2016;29(July):1–18.
10. Koşar A, Peles Y. Micro scale pin fin heat sinks—parametric performance evaluation study. IEEE Trans Compon Packag Technol. 2007;30(4):855–65.
11. Izci U, Koz M, Koşar A. The effect of micro pin-fin shape on thermal and hydraulic performance of micro pin-fin heat sinks. Heat Transf Eng. 2015;36(17):1447–57.
12. Koşar A, Schneider B, Peles Y. Hydrodynamic characteristics of crossflow over MEMS-based pillars. J Fluids Eng. 2011;133(8):081201(1–11).
13. Rubio-Jimenez CA, Kandlikar SG, Hernandez-Guerrero A. Numerical analysis of novel micro pin fin heat sink with variable fin density. IEEE Trans Compon Packag Manuf Technol. 2012;2(5):825–33.
14. Gonzalez-Hernandez JL, Kandlikar SG, Hernandez-Guerrero A. Performance assessment comparison of variable fin density microchannels with offset configurations. Heat Transf Eng. 2016;37(16):1369–81.
15. Liu Z, Zhang C, Guan N. Experimental investigation on resistance characteristics in micro/mini cylinder group. Exp Therm Fluid Sci. 2011;35(1):226–33.
16. Roth R, Cobry K, Lenk G, Woias P. Micro process engineering of freestanding silicon fluidic channels with integrated platinum thermistors for obtaining heat transfer correlations. In: 8th Annual IEEE international conference on nano/micro engineered and molecular systems (NEMS 2013), pp 879–882.
17. John TJ, Mathew B, Hegab H. Parametric study on the combined thermal and hydraulic performance of single phase micro pin-fin heat sinks part I: square and circle geometries. Int J Therm Sci. 2010;49:2177–90.
18. Liu Z, Wang Z, Zhang C. Flow resistance and heat transfer characteristics in micro-cylinders-group. Heat Mass Transf. 2013;49:733–44.

19. Bahiraei M, Heshmatian S, Keshavarzi M. Multi-criterion optimization of thermohydraulic performance of a mini pin fin heat sink operated with ecofriendly graphene nanoplatelets nanofluid considering geometrical characteristics. J Mol Liq. 2019;276:653–66.
20. Bahiraei M, Heshmatian S. Optimizing energy efficiency of a specific liquid block operated with nanofluids for utilization in electronics cooling: a decision-making based approach. Energy Convers Manag. 2017;154(August):180–90.
21. Mohammadi A, Koşar A. Hydrodynamic and thermal performance of microchannels with different in-line arrangements of cylindrical micro pin fins. J Heat Transf. 2016;138(12):122403 (1–17).
22. Mohammadi A, Koşar A. Hydrodynamic and thermal performance of microchannels with different staggered arrangements of cylindrical micro pin fins. Heat Transf. 2017;139(6):062402 (1–13).
23. Kandlikar SG. Heat transfer and fluid flow in minichannels and microchannels. Amsterdam: Elsevier; 2006.
24. Li Z, Huai X, Tao Y, Chen H. Effects of thermal property variations on the liquid flow and heat transfer in microchannel heat sinks. Appl Therm Eng. 2007;27:2803–14.
25. Lee DH, Rhee DH, Kim KM, Cho HH, Moon HK. Heat transfer and flow temperature measurements in a rotating triangular channel with various rib arrangements. Heat Mass Transf. 2009;45(12):1543–53.